A Comparative Study of Two Methods for the Correction of Beam Hardening Artifacts in X-ray Computed Tomography

by

Maryam Khalid Alarfaj

submitted to
Oregon State University

in partial fulfillment of
the requirements for the
degree of

Master of Science

December 2012

Abstract

The polychromatic energy spectrum of common x-ray sources causes so-called beam hardening artifacts in x-ray computed tomography images. The artifacts typically contain dark streaks and overall cupping. In this paper we compare two methods for reducing such artifacts. A correction method proposed by Herman and Trivedi in 1985, and an iterative correction method by G. Van Gompel et al. in 2011. We describe and implement both correction methods and provide numerical experiments for comparison.

Acknowledgments

I would like to gratefully thank my advisor Dr. Adel Faridani for his continuous support, guidance and patience.

My sincere thanks also go to Dr. Donald Solmon for inspiring and encouragemen.

A special gratitude goes to my family. Words can not express how grateful I am to my parents. I m thankful to my brother Mohammed for all his care and affection.

Chapter 1

Introduction

1.1 X-ray computed tomography

Over the past 45 years, the problem of image reconstruction from projections has taken a large space among many different research fields such as science, medicine and technology. This problem is referred to as computed tomography. 1979 Nobel Prize for Physiology or Medicine was awarded to A. Cormack and G. Hounsfield for the development of x-ray computed tomography(CT) [6]. X-ray CT is an x-ray modality used to generate a two dimensional cross sectional image of the human body from two dimensional x-ray projections. Later, the method has been extended to generate a three dimensional image. In this paper, we consider the two dimensional case. Mathematically, tomography means reconstruction of a function from it's line integrals.

There are different types of artifacts that may corrupt the x-ray image. Some artifacts are caused by the patient itself. For example, the motion artifact which occurs when the patient moves during the acquisition, and the metal artifact which results from having metallic dental fillings or implants. Another type of artifact results from an x-ray source that emits x-rays of multiple energies. This is called a beam hardening artifact.
Reducing beam hardening artifacts has become an active research field in x-ray CT. As a result, a variety of methods have been proposed for correction. Some methods do not require prior knowledge of the material properties, for example [7, 8]. The scope of this paper is to present a comparative study of two methods for the correction of beam hardening artifact in CT images .

This paper is organized as follows. In this chapter, we introduce the physics of beam hardening and analyze the problem. In chapter 2, we describe a correction method presented by Herman and Trivedi [3]. Chapter 3 presents an iterative correction method developed by G. Van Gompel et al. in [4]. A concluding chapter contains a comparison and discussion of the methods.

1.2 The problem of beam hardening

The goal of tomography is to reconstruct the density function inside an object from the rays which pass through the object. This density function μ is the linear x-ray attenuation coefficient and depends on the spatial coordinates (x, y) in the cross section and on the x-ray energy distribution (spectrum) E, so it can be denoted as $\mu(x, y, E)$.

Under the assumption of an ideal monochromatic ray source, i.e, a spectrum of only one level of energy $\bar{E}$, the physical effect of attenuation is described by Beer's law

$$I_D = I_0 \, e^{-\int_L \mu(x,y) \, ds} \tag{1}$$

where L represents the straight line which is the path of the ray, I_0 is the initial intensity of the ray at the source, and I_D is the detected intensity of the ray after going through the object. For this beam, we can define the monochromatic ray sum, the measurement, M, as

$$M = -\ln \frac{I_D}{I_0}. \tag{2}$$

We can estimate the line integral of μ from the measurement, if we assume that the photons of the ray have the same level of energy. We get a linear relationship between the measurement and the line integral and equation (1) implies that,

$$M = \int_L \mu(x, y) \, ds \tag{3}$$

The first image shown in Figure 1 is a 200×200 density phantom used to illustrate the problem of beam hardening. The phantom is produced at 61 keV with a large disk of brain and four disks of bone. The location of each disk is described by two variables, the center of the disk (X, Y), and the radius R as shown in Table 1. The energy spectrum and the corresponding linear attenuation coefficient for each material are described in Table 2 obtained from [2]. We denote the grey scale window by an interval $[a, b]$. By this we mean that values in the image that are less than or equal to a are displayed as black, and values greater than or equal to b are displayed as white. Values in the interval are displayed with a corresponding scale of grey. We will use the interval [0.15,0.22] unless otherwise noted. All the pictures

display the function in the square $[-1, 1]^2$.

The reconstruction shown in the bottom left of Figure 1 is created from the ideal monochromatic data at 61 keV by exactly computing the line integral in equation (3). By comparison, the reconstruction looks similar to the original phantom with no artifact. So if we plot a line through the image, the resultant density profile appears as a constant as shown in the bottom right of Figure 1.

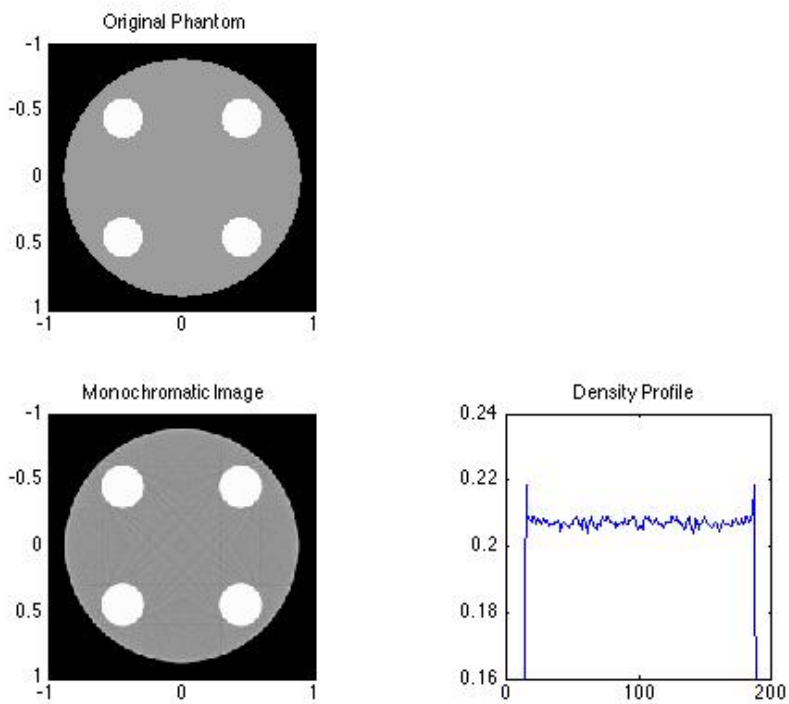

Figure 1: Illustration of the reconstruction from the ideal monochromatic data at 61 keV. The grey window scale is [0.17,0.24]. **Top**: True image of 200×200 pixels for a cross sectional mathematical phantom made of a large disc of brain and four small discs of bone, the density values are in Table 1. **Bottom left**: A reconstruction from the ideal monochromatic data at 61 keV which looks similar to the original phantom. **Bottom right**: The corresponding density profile of row number 120 for the monochromatic reconstruction which is nearly constant. The grey scale window is [0.15,0.22].

However, in reality we have a polychromatic ray source where the x-ray beam is made up of photons of different energies. So the relationship between the initial intensity and the detected intensity will be modeled by the more complicated equation,

$$I_D = I_0 \int_0^\infty \tau(E)\, e^{-\int_L \mu(x,y,E)\, ds}\, dE \tag{4}$$

where $\tau(E)$ is the probability density that the detected photon is at energy E.

For this beam, we define the measured uncorrected polychromatic data P^{meas}, along a line L, as

$$P^{meas} = -\ln \frac{I_D}{I_0} \tag{5}$$

$$P^{meas} = -\ln \int_0^\infty \tau(E)\, e^{-\int_L \mu(x,y,E)\, ds}\, dE \tag{6}$$

and for each pair of source and detector we use P^{meas} to denote the line integral of μ along the line L, i.e, the measured polychromatic data.
Clearly, taking the logarithm as before does no longer give a linear relationship between the unknown μ and the measurement P^{meas}. So if we reconstruct using these nonlinear data by the inversion algorithm for the monoenergetic data, we will get an artifact caused by the nonlinearity. This artifact is called beam hardening artifact.

Physically a harder beam contains a higher proportion of high energy photons. The x-ray beam used in CT is composed of photons with different levels of energy (polyenergetic). When the x-ray passes through the object of interest, the photons of higher energy will be attenuated less than the lower energy photons. As a result, the beam becomes harder when it reaches the detector. Two types of artifacts can result from this phenomenon as seen in Figure 2. Dark streaks appear between high density objects such as bone as shown in the bottom left of Figure 2. Cupping artifact where we get lower values inside as shown in the right of Figure 2. So if we plot a cross line through the image instead of getting a constant it will look like a cup, because the beam becomes harder in the center of the object (see Figure 2.)

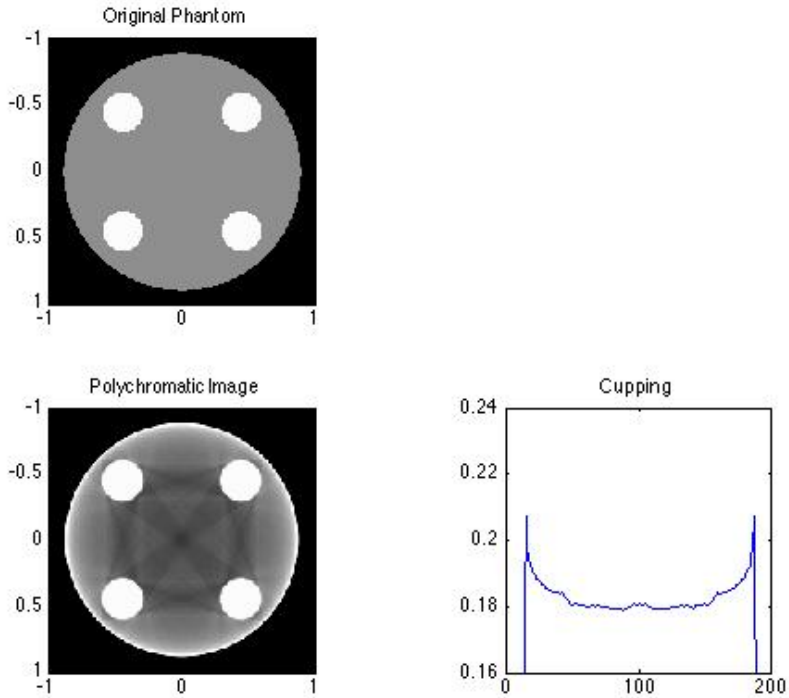

Figure 2: Illustration of beam hardening artifacts. **Top**: The original phantom as in Figure 1. **Bottom left**: A reconstruction from the uncorrected polychromatic data with beam hardening artifact: dark streaks can be found between the four disks of bone, and lower values inside (cupping artifact). **Bottom right**: The density profile of row number 120 in the uncorrected image shows the cupping artifact. The grey scale window is [0.17,0.20].

1.3 Simulation for polychromatic projection data

In our simulation, we use a mathematical phantom made up of ellipses as shown in Figure 1. We generate the measured polychromatic data, P^{meas}, by approximately replacing the outer integral for the continuous energy spectrum in equation (6) by a discrete spectrum consisting of k energies E_1, E_2,....., E_k. We can compute the exact inner integral $\int_L \mu(x, y, E_k)\, ds$ since $\mu(x, y, E_k)$ is a linear combination of characteristic functions of ellipses. Thus equation (6) is replaced by,

$$P^{meas} = -\ln \sum_k \tau(E_k)\, e^{-\int_L \mu(x,y,E_k)\, ds}\, \Delta E_k \tag{7}$$

where $\tau(E_k)\Delta E_k$ is the probability that the detected photon is at energy E_k.

Table 1: Description of the location parameters used to produce the original phantom in Figure 1

Disk No.	X	Y	R
1	0	0	0.9
2	-0.45	0.45	0.15
3	0.45	0.45	0.15
4	-0.45	-0.45	0.15
5	0.45	-0.45	0.15

Table 2: The x-ray spectrum and attenuation values used in the experiments

E_k (keV)	$\tau(E_k)$	Bone	Brain	Metastatic breast carcinoma	Soft Tissue 1	Soft Tissue 2
41	0.1	0.999	0.265	0.288	0.357	0.448
52	0.3	0.595	0.226	0.241	0.272	0.3182
61	0.3	0.416	0.210	0.220	0.236	0.261
80	0.2	0.265	0.183	0.190	0.193	0.203
100	0.1	0.208	0.174	0.179	0.178	0.182

Chapter 2

A Correction Method by Herman and Trivedi

Several techniques have been proposed to eliminate beam hardening artifacts in x-ray images. In this chapter we describe a post-reconstruction method which was first developed by Joseph and Spital [10], but we follow a presentation by Herman and Trivedi [3]. The method aims to generate artificial monochromatic data from the polyenergetic ray sum. This method requires prior knowledge of the x-ray spectrum and identification of the bone pixels from an initial reconstruction, for example by the filtered back projection algorithm, (FBP). The method consists of two stages of correction. The first stage of correction assumes that only soft tissue is present in the image. The second stage is the final correction and allows for the presence of both soft tissue and bone. The two stages are working well in certain conditions. We conduct some numerical experiments to test the efficiency of each stage.

2.1 The First Stage of Correction- Soft Tissue Correction

The first stage of correction is a soft tissue correction which partially corrects for beam hardening. It is carried out under the assumption that the body consists of only soft-tissue material. It is assumed that the pixels contain soft tissue with known linear attenuation coefficient $\mu^{soft}(E)$ for all energies in the spectrum. In this stage, the goal is to reconstruct an initial reconstruction $\mu^{soft}(\bar{E})$ which has been corrected partially for beam hardening from the uncorrected data P^{meas}. For that we find the length of intersection of each ray with the soft tissue T_s to generate artificial monochromatic data M, where

$$M = \mu^{soft}(\bar{E})\ T_s\ . \tag{8}$$

Since we assume that the body is made of uniformly soft tissue,

$$\mu(x, y, E) = \begin{cases} \mu^{soft}(E) & \text{if (x,y) in the object} \\ 0 & \text{if (x,y) out the object} \end{cases}$$

so we can simplify the line integral of μ as,

$$-\int_L \mu(x, y, E)\, ds = -\mu^{soft}(E)\, T_s\ . \tag{9}$$

Now T_s is determined such that the simulated data computed by using equation (9) match the measured data.
Inserting equation (9) in equation (7) gives a non-linear equation for T_s that we can solve numerically:

$$-\ln \sum_k \tau(E_k)\, e^{-\mu^{soft}(E_k)\, T_s}\ \Delta E_k = \ P^{meas}.$$

This equation has to be solved for every line L for which measured data are available. After finding T_s we can compute the artificial monochromatic data M according to equation (8) and reconstruct the image of the first stage correction.

Figure 3 illustrates the result after applying the first stage of correction on the uncorrected polychromatic data. The energy level $\bar{E}$ has chosen to be 61 keV (see Table 2). The corresponding density profile of the corrected image shows that the soft-tissue correction works well in reducing the cupping artifact, however, the dark streaks are still present between the four disks of bone. Therefore, we can say that the first stage of correction sufficiently corrects the cupping artifact but not the streaks.

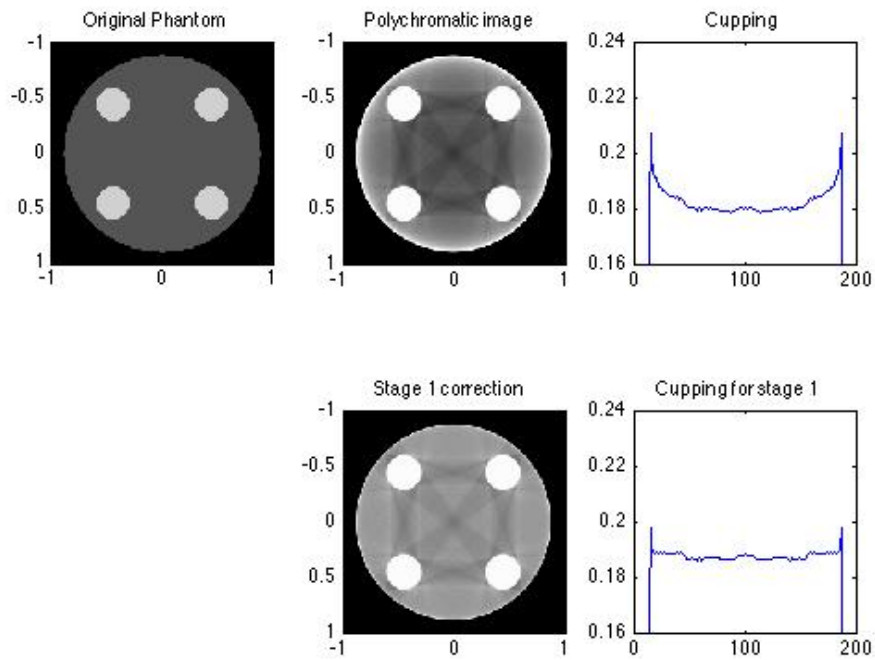

Figure 3: **Top left**: Illustration for the first stage correction. The original phantom as in Figure 1. **Top center**: Uncorrected reconstruction from polychromatic data with beam hardening: dark streaks and cupping artifact. **Top right**: The corresponding density profile of row number 120 for the uncorrected image shows the cupping artifact. **Bottom center**: A reconstructed image by the first stage correction shows reducing the cupping artifact while the dark streaks are present, where $\mu^s(\bar{E}) = 0.19$. The grey window scale is [0.17,0.20]. **Bottom right**: The first stage reduced the cupping artifact as shown in the density profile of row number 120.

2.2 The Second Stage of Correction

The second stage is the final stage of correction which allows for the presence of both soft tissue and bone in the image. As we see, the first stage works well with the assumption of one material, but in reality the

human body is made up of different layers and tissues so the first stage is not sufficient for a full correction. In the second stage, we assume that the body consists of soft tissue and bone with known linear attenuation coefficients $\mu^s(E)$ and $\mu^b(E)$ respectively for all energies in the spectrum. The goal of the second stage is to find the lengths of intersection T_b and T_s of each ray with the bone and soft tissue, respectively, in order to generate artificial monochromatic data M where

$$M = \mu^s(\bar{E})T_s + \mu^b(\bar{E})T_b \tag{10}$$

In order to estimate T_b, we segment the reconstructed image from the first stage by thresholding. To perform the segmentation, we choose the pixels from the first stage image whose values are above 0.210. These pixels are assumed to contain bone. Figure 4 shows the segmented bone image. This is a binary image where the pixels assumed to contain bone have the values 1 and the other pixels are set to zero. Then we estimate T_b by taking the

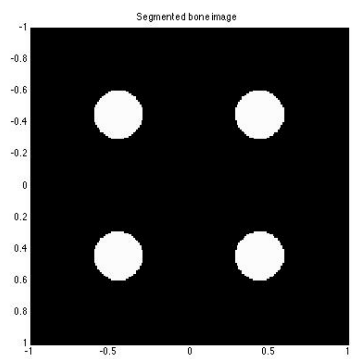

Figure 4: The segmented bone image

line integrals for this segmented bone image. In the method of Herman and Trivedi, T_b was computed by finding the actual length of intersection of the ray with each pixel. However, in our implementation, we apply MATLAB's Radon command to approximate the X-ray transform of the image [5]. The idea to use this algorithm is adapted from N. Resvani's recent Ph.D. thesis [8]. It is a fast and direct way to compute the simulated polychromatic data. The algorithm is described by the MathWorks as follows "The radon transform of an image in MATLAB is the sum of the radon transform for all the pixels in

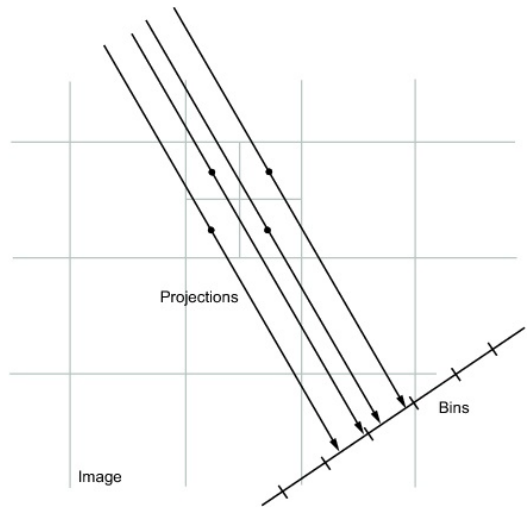

Figure 5: MATLAB's radon function divides each pixel into four sub-pixels and projects each sub-pixel separately. This picture is taken from http://www.mathworks.com/help/images/ref/radon.html.

the image. The algorithm first divides each pixel in the image into four sub-pixels and projects each sub-pixel separately as shown in Figure 5. Each sub-pixel's contribution is proportionally split into the two nearest bins, according to the distance between the projected location and the bin centers. If the sub-pixel projection hits the center point of a bin, the bin on the axes gets the full value of the sub-pixel, or one-fourth the value of the pixel. If the sub-pixel projection hits the border between two bins, the sub-pixel value is split evenly between the bins."
After finding T_b, we solve this nonlinear equation for the unknown T_s,

$$\begin{aligned} P^{meas} &= -\ln \int_0^\infty \tau(E)\, e^{-\mu^s(E)T_s - \mu^b(E)T_b}\, dE \\ &\simeq -\ln \sum_k \tau(E_k)\, e^{-\mu^s(E_k)T_s - \mu^b(E_k)T_b}\, \Delta E_k \end{aligned}$$

Then we combine these values to get the artificial monochromatic data according to equation (10).

Figure 6 shows a comparison between the polychromatic image before the correction and after the second stage of correction. The second stage

works successfully in reducing the dark streaks and the cupping artifact. The resultant density profile from the second stage shows an improvement in making the line more constant. Indeed, the two stages of Herman and Trivedi works well in reducing beam hardening artifact for an object of two uniform materials (soft tissue and bone.)

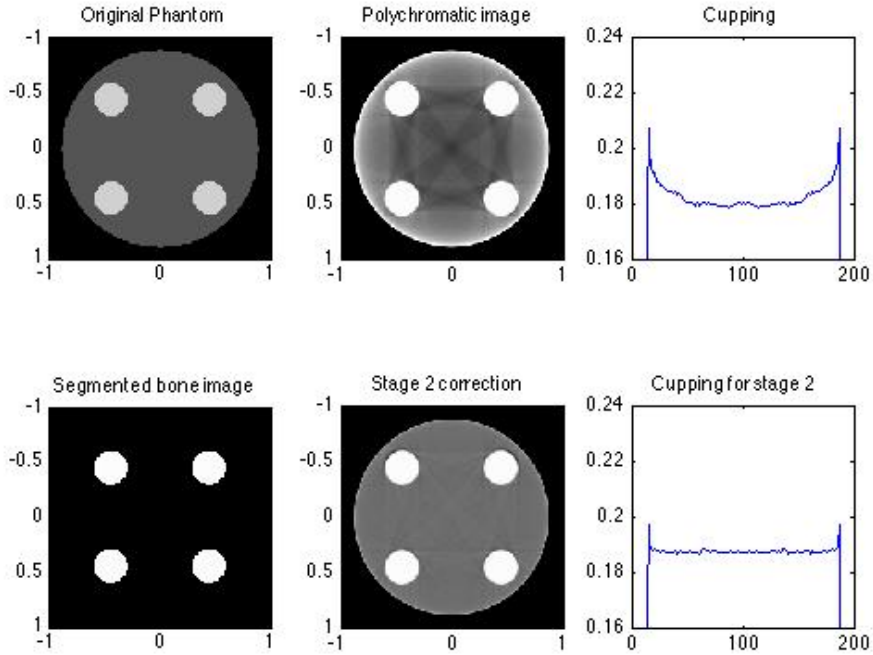

Figure 6: Illustration of the second stage correction. **Top left**: The original phantom as in Figure 1. **Top center**: Uncorrected reconstruction from polychromatic data where beam hardening can be found: dark streaks and cupping artifact. **Top right**: The corresponding density profile of row number 120 of the uncorrected image shows the cupping artifact. **Bottom left**: The segmented bone image is obtained by thresholding the first stage reconstructed image. The threshold value is 0.210. **Bottom center**: A reconstructed image by the second stage correction shows removing the dark streaks, where $\mu^s(\bar{E}) = 0.19$ and $\mu^b(\bar{E}) = 0.23$. The grey scale window is [0.17,0.21]. **Bottom right**: The corresponding density profile of row number 120 of the second stage image shows reduction of the cupping artifacts.

2.3 Experiments and Results

Is the first stage necessary? Our phantom is perhaps too simple to determine that but we might try to do the correction without the first stage. Figure 7 shows the performance of the second stage without using the first stage correction. In this experiment, we segment our initial uncorrected polychromatic image for bone. Because of cupping the values near the boundary of the large disc are elevated and appear in the segmentation as bone. However, using the first stage of correction helps in removing the cupping which gives a better chance to accurately identify the bone. Thus, using the first stage is helpful to get a better segmentation for the bone and then a correct result.

The method of Herman and Trivedi removed the beam hardening artifact successfully on a phantom of two materials. So, one possible experiment is to test the quality of the method on a phantom made of more than two materials. For examination, we use our original phantom as in Figure 1, but we add a small disk of a third different material (Metastatic breast carcinoma in Table 2) in the center of the phantom. Figure 8 shows that when we run the reconstruction algorithm without any correction, the new soft tissue becomes invisible since the dark streaks intersect in the middle where the third material is. The cupping artifact is also shown when we plot a line through the uncorrected image. However, if we run the two stages for correction, the beam hardening artifact is successfully suppressed which makes the third material more visible. The result indicates that the method of Herman and Trivedi works well on more than two materials.

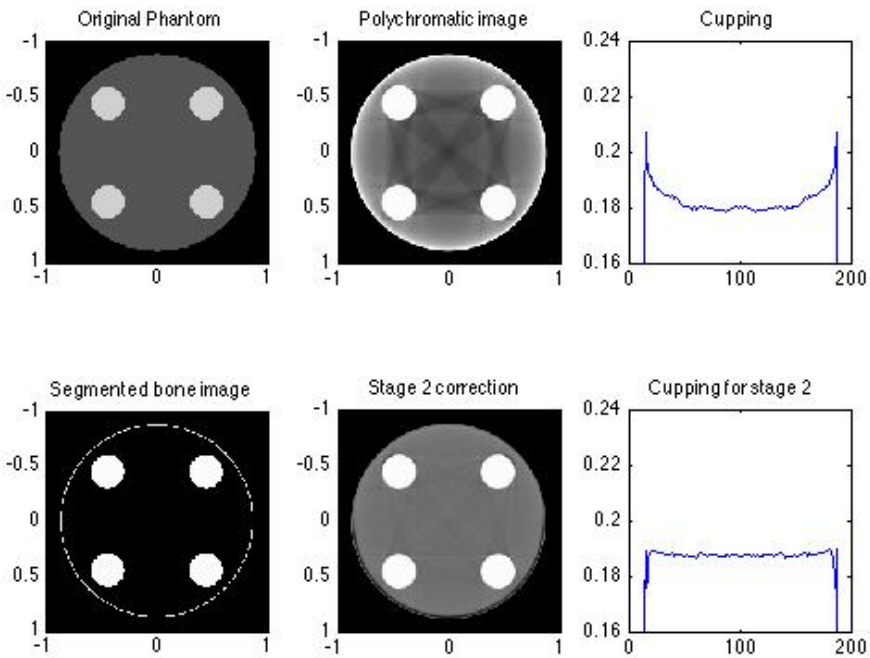

Figure 7: The performance of the second stage correction without using the first stage for segmentation. **Top left**: The original phantom as in Figure 1. **Top center**: Uncorrected reconstruction from polychromatic data. **Top right**: The corresponding density profile of row number 120 of the uncorrected image shows the cupping artifact. **Bottom left**: Poor segmentation results from segmenting the uncorrected polychromatic image where a white ring can be found. The threshold value is 0.210. **Bottom center**: A reconstruction for the second stage correction, where $\mu^s(\bar{E}) = 0.19$ and $\mu^b(\bar{E}) = 0.23$. The grey scale window is [0.17,0.21]. **Bottom left**: The corresponding density profile of row number 120 of the second stage.

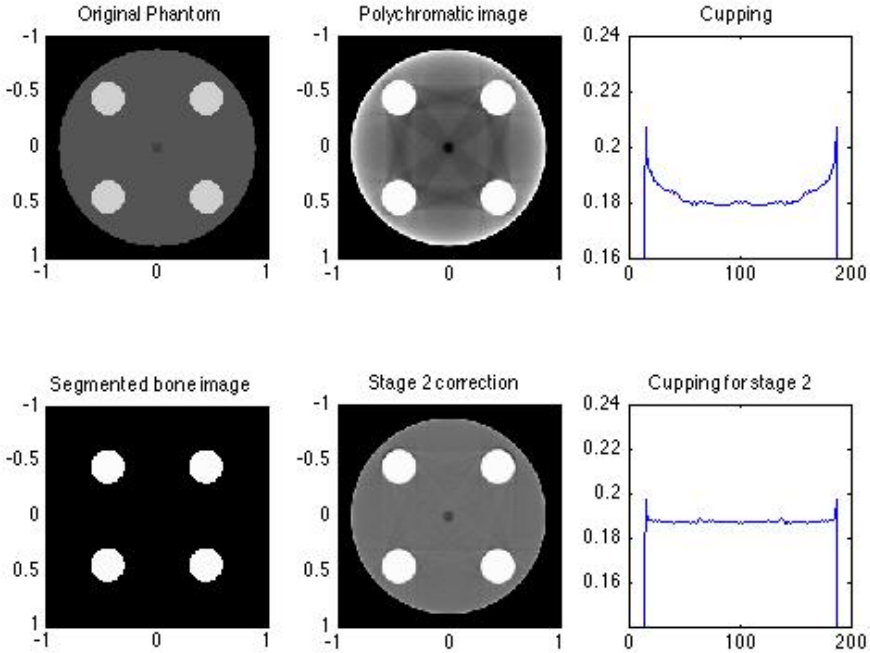

Figure 8: Illustration of the method of Herman and Trivedi on three materials. **Top left**: Our original phantom with an additional small disk for a third different material placed in the center. **Top center**: A reconstruction from the uncorrected polychromatic data with beam hardening artifact. **Top right**: The density profile of row number 120 in the uncorrected image shows the cupping artifact. **Bottom left**: A segmented bone image by thresholding. The threshold value is 0.210. **Bottom center**: A reconstruction after applying the two stages of correction, where $\mu^s(\bar{E}) = 0.19$ and $\mu^b(\bar{E}) = 0.23$. Streaks are removed which make the third material in the middle more visible. **Bottom right**: The corresponding density profile of row number 120 of the second stage image shows reducing the cupping artifact. The grey scale window is [0.17,0.21]

Chapter 3

Iterative Correction Method

Recently, G. Van Gompel, K. Slambrouck, M. Defrise, K. Batenburg, J. Mey, J. Sijbers, and J. Nuyts proposed an iterative correction method for beam hardening artifacts [4]. The method does not require prior knowledge about spectrum or materials. This is considered to be a practical advantage compared to many other correction algorithms which require information about spectrum and materials. Herman and Trivedi's method, although our experiment indicates that the method may work if there are more than two materials, is designed to handle only two different materials except air. There is bone and everything else is soft tissue. However, the present method does not have this limitation. It can handle an arbitrary number of materials. It assumes that the object consists of a known number of materials. It requires segmentation of an initial FBP image which is usually obtained from uncorrected polychromatic data. It does not require the materials to be uniform, unlike Herman and Trivedi's method and some other methods which do assume uniform materials [9, 10]. This method aims to reconstruct an image where simulated polychromatic data which are computed from this image match the measured polychromatic data as closely as possible.
Three iterative algorithms based on this approach are presented by G. Van Gompel et al. in [4]. In this paper we describe two of these algorithms: the iterative filtered back projection approach (IFR), and the sinogram preprocessing method (ISP).

3.1 Assumption and Concepts

Let N be the known number of different materials in the object. Let D denote the total number of x-ray projection lines, and J the number of pixels in the image. The method assumes that each pixel contains only one material. Let $s_{n,j}$ be the jth pixel of the segmented image for material number n, that is $s_{n,j} = 1$ if pixel j is occupied by material n, and $s_{n,j} = 0$ otherwise. Let define $\mu_n(E_k)$ to be an approximation of the average linear attenuation coefficient of material n at energy E_k. Since the method can deal with slightly non-uniform materials, let us introduce a relative density parameter, d_j which

models the small variation in x-ray attenuation within one class of material for pixel j. The attenuation at pixel j for energy E_k is then given by:

$$R_{j,k} = d_j \sum_{n=1}^{N} \mu_n(E_k)\, s_{n,j} \tag{11}$$

The line integral of the discretized image along line i at energy E_k is given by

$$\begin{aligned} L_{i,k} &= \sum_{j=1}^{J} l_{i,j}\, R_{j,k} \\ &= \sum_{n=1}^{N} \mu_n(E_k) \sum_{j=1}^{J} d_j\, l_{i,j}\, s_{n,j} \end{aligned} \tag{12}$$

where $l_{i,j}$ denotes the length of intersection of line i with the jth pixel. Therefore, the simulated polychromatic data for line i are given by:

$$\begin{aligned} P_i^{sim} &= P_i^{sim}(\mu, \tau, d, s) \\ &= -\ln \sum_{k=1}^{K} \tau(E_k)\, e^{-L_{i,k}} \Delta E_k \\ &= -\ln \sum_{k=1}^{K} \tau(E_k)\, e^{-\sum_{n=1}^{N} \mu_n(E_k) \sum_{j=1}^{J} l_{i,j}\, d_j\, s_{n,j}} \Delta E_k \end{aligned} \tag{13}$$

The approach aims to compute an image where the discrepancy between the measured polychromatic data, P_i^{meas} and the simulated polychromatic data, P_i^{sim} is minimized, i.e, it aims to iteratively minimize a cost function, $\phi(\mu, \tau, d, s)$ to produce an image with reduced beam hardening artifacts. The cost function is given by:

$$\begin{aligned} \phi(\mu, \tau, d, s) &= \frac{1}{D} \sum_{i=1}^{D} (\, P_i^{meas} - \, P_i^{sim})^2 \\ &= \frac{1}{D} \sum_{i=1}^{D} \left(\ln \frac{I_D}{I_0} - \ln \left(\sum_k \tau(E_k)\, e^{-\sum_{n=1}^{N} \mu_n(E_k) \sum_{j=1}^{J} l_{i,j} d_j\, s_{n,j}} \Delta E_k \right) \right)^2 \end{aligned}$$

In our implementation, we apply MATLAB's Radon command [5] to approximate the quantity $\sum_{j=1}^{J} l_{i,j}\, d_j\, s_{n,j}$ occurs in the expression (12) for the line integral $L_{i,k}$.

3.2 Iterative filtered back projection (IFR)

The IFR approach follows an optimization procedure to minimize the cost function iteratively. The IFR starts with an initial reconstruction that is obtained from the measured polychromatic data, $R^0 = FBP(P^{meas})$, where $FBP(P^{meas})$ denotes an image that is computed from the data P^{meas} with the filtered back projection algorithm. It assumes that the object consists of N materials. In each iteration w, the following steps are performed:

3.2.1 Update of the segmentation

We estimate the parameter $s^w_{n,j}$ by thresholding the current image R^{w-1} into N segments in a way that minimizing the cost function. Since the gradient of the cost function with respect to the threshold is often near zero, we encountered difficulties using the standard optimization software in MATLAB for finding the threshold values that minimize the cost function. The cost function only changes significantly at points where the threshold is near a density of one of the materials. Then if we change the threshold a little bit, the segmentation changes. But if the threshold is away from one of the material's densities then by changing the threshold a little bit, the segmentation and therefore the cost function remains the same. For that reason, we used an ad hoc method devised by A. Faridani for finding a reasonable initial threshold where the gradient of the cost function is not zero. Let $F(x)$ be the number of pixels in the current image with density less than or equal to x. As x increases, we get more pixels where the image is less than x so $F(x)$ is increasing. $F(x)$ changes most rapidly when x is near the density of one of the materials. Therefore we set the maxima of $F'(x)$ to find good starting values for the thresholds. Here $F'(x)$ denotes a numerical derivative. Then we use a simple gradient descent method to find threshold values that decreases the cost function by searching along the direction of the negative

gradient.

3.2.2 Update of the relative density

In the first iteration $w = 1$ we initialize the relative density by one, i.e, $d_j = 1$ for all the pixels. For the next iteration, $w > 1$ we compute the updated relative density by:

$$d^w = d^{w-1} + \omega^w.FBP(\ P^{meas} -\ \ P^{sim}(\mu^{w-1}, \tau^{w-1},\ d^{w-1}, s^w))$$

where ω^w is a relaxation factor with elements

$$\omega_j^w = \frac{1}{\sum\limits_{n=2}^{N} \mu_{IFR,n}^w\, s_{n,j}}$$

where $\mu_{IFR,n}^w = \max\{\mu_n^{w-1}(E_1), ..., \mu_n^{w-1}(E_k)\}$, and P^{sim} is computing according to equation (13).

3.2.3 Attenuation and the fractional Intensity

The updated s and d are fixed and the optimization procedure is performed for the unknowns μ and τ to minimize the cost function. This is done in the paper by G. Van Gompel et al., but in our implementation we use the actual values in our simulation as shown in Table 2.

3.2.4 Image Update

After estimating all the reconstruction parameters(μ, τ, d, s), we compute the updated image, R^w to find the segmentation for the next iteration:

$$R^w = d_j^w \sum_N \mu^w(E_k) s_{n,j}^w$$

Thus, the iteration is terminated if the simulated polychromatic data are sufficiently close to the measured data. Then G. Van. Gompel et al. suggest the following stopping criterion:

$$\frac{\epsilon^w + \epsilon^{w-1}}{\epsilon^{w-2} + \epsilon^{w-3}} >\ t$$

where the polychromatic model error ϵ^w is the value of the cost function $\phi(\mu^w, \tau^w, d^w, s^w)$. For the next iterations $w > 1$, we compute the new threshold from the updated image that minimizes the cost function.
for segmentation and display purposes, we choose

$$R^w = d_j^w \sum_N \bar{\mu}_{IGR,n}^w s_{n,j}^w$$

where $\bar{\mu}_{IGR,n}^w$ is chosen to be the median of $\{\mu_n^w(E_1), ..., \mu_n^w(E_k)\}$.

3.3 Sinogram Preprocessing Method (ISP)

In the IFR, the relative density is estimated in each iteration for each pixel and the image is updated by minimizing the discrepancy between the simulated data and the measured data. In the ISP algorithm, the authors of [4] suggest to set the relative density to one in all the pixels to eliminate the presence of noise. The ISP algorithm starts with an initial reconstruction which is obtained from the measured polychromatic data, $R^0 = FBP(P^{meas})$. In each iteration w, we perform the following steps:

3.3.1 Update of the segmentation

We follow the IFR algorithm to update the parameters $s_{n,j}$.

3.3.2 Attenuation and the fractional Intensity

The updated s and d are fixed and the optimization procedure is performed for the unknowns μ and τ to minimize the cost function. In in our implementation we use the actual values in our simulation as shown in Table 2.

3.3.3 Mono- and polychromatic simulation

The monochromatic and polychromatic simulated data are computed as the follows, respectively

$$M_i^{sim,\ w} = \sum_{n=1}^{N} \bar{\mu}_{ISP,n}^w \sum_{j=1}^{J} l_{i,j}\, s_{n,j}^w \tag{14}$$

$$P_i^{sim,\ w} = -\ln \sum_{k=1}^{K} \tau(E_k)\, e^{-\sum_{n=1}^{N} \mu_n^w(E_k) \sum_{j=1}^{J} l_{i,j}\, s_{n,j}^w} \Delta E_k \tag{15}$$

where the reference attenuation coefficients $\bar{\mu}_{ISP,n}^w$ in (14) are determined below.

3.3.4 Sinogram Correction and Image Update

The corrected monochromized sinogram, $M^{corr,\ w}$ is obtained by adding the correction term $(M_i^{sim,\ w} - P^{sim,\ w})$ to the original polychromatic data P^{meas}

$$M^{corr,\ w} = P^{meas} + (M^{sim,\ w} - P^{sim,\ w}) \tag{16}$$

Then, for the next iteration, the updated image will be $R^w = FBP(M^{corr,\ w})$.

Reference Attenuation

In order to generate monochromatic data, the authors suggest to choose attenuation values that minimize the magnitude of the correction term in equation (16). The theoretical reason is that when the segmentation considers two low contrast materials as one material, the information that allows to discriminate there materials is contained only in the measured data. A smaller correction here may be less likely to obscure this information. Thus, to better visualize the discrimination in the updated image, the reference attenuation coefficient $\bar{\mu}_{ISP,n}^w$ has to minimize the function $\Psi(\bar{\mu}_{ISP}^w)$,

$$\begin{aligned} \Psi(\bar{\mu}_{ISP}^w) &= \sum_{i}^{D} (M_i^{sim,\ w} - P^{sim,\ w})^2 \\ &= \sum_{i}^{D} \left(\sum_{n=1}^{N} \bar{\mu}_{ISP,n}^w\, t_{n,i}^w + \ln \sum_{k=1}^{K} \tau(E_k)\, e^{-\sum_{n=1}^{N} \mu_n^w(E_k)\, t_{n,i}^w} \right)^2 \end{aligned}$$

where

$$t_{n,i}^w = \sum_{j=1}^{J} l_{i,j}\, s_{n,j}^w$$

Thus, the minimum of $\Psi(\bar{\mu}_{ISP}^w)$ is given by,

$$\bar{\mu}_{ISP}^w = B^{w+} v^w$$

where B^{w+} is the pseudo inverse of the matrix B with elements,

$$b_{n,m} = \sum_{i}^{D} t^{w}_{n,i} t^{w}_{m,i}$$

for n,m = 1,...,N, and v^w is the vector with entries:

$$v^{w}_{m} = -\sum_{i}^{D} t^{w}_{m,i} \ln \sum_{k=1}^{K} \tau(E_k)\, e^{-\sum\limits_{n=1}^{N} \mu^{w}_{n}(E_k)\, t^{w}_{n,i}}$$

for m = 1,...,N.

3.4 Experiments and Results

Figure 9 shows an image of 200×200 pixels of the original phantom that we used to test the algorithms on more than two uniform materials. The phantom is produced at 61 keV with 5 different materials ($N = 5$): air, a large disk of brain, two small upper disks of bone, and two small lower disks with two low contrast materials of soft tissues, soft tissue 1 and soft tissue 2. The location parameters for each disc and the attenuation values of each material are provided in Tables 1 and 2 respectively. This phantom is similar to the one that we used in the method of Herman and Trivedi, but we used two low contrast soft tissues instead of the two lowest disks of bone, since the iterative algorithm allows for more than two materials.

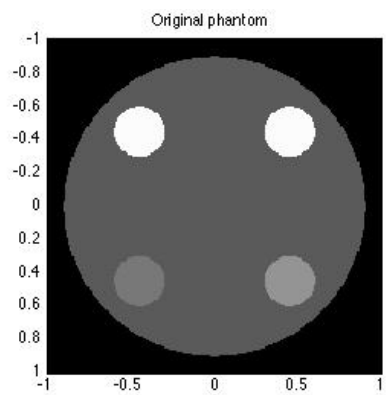

Figure 9: True image of 200×200 pixels for a cross sectional mathematical phantom made of (5 materials including air) a large disc of soft brain, two small upper discs of bone, and two small disks with low contrast materials of soft tissues, disc number 4 of soft tissue 1 and disc number 5 of soft tissue 2. The location of each disk and the attenuation values are described in Tables 1 and 2 respectively. The grey scale window is [0.13,0.35].

Figure 10 illustrates the performance of the iterative algorithms IFR and ISP using four iterations. It can be observed from the updated images that the iterative algorithms significantly reduce the beam hardening artifacts relative to the uncorrected polychromatic image. IFR and ISP successfully remove the dark streaks between bones. IFR produces a sharper but more noisy image than the low resolution ISP. A white ring at the outer boundary of the object is present in IFR and ISP . The corresponding profile plots of the corrected images further show the difference in performance between the two methods. We insert a horizontal line through the lower two discs to compare how each method can deal with two low contrast materials of soft tissues. In comparison, IFR gives a better contrast between the two low contrast soft tissues than ISP due to the relative density parameter in IFR. In addition, we quantify the performance of the two iterative algorithms using the cost function values after each iteration as shown in Table 3. Both IFR and ISP tend to decrease the cost function although with the ISP there is occasional increase. Indeed, ISP does not guarantee to decrease the cost function when we update the image. After further iterations, the IFR continues to decrease the cost function but this results in producing a noisy picture. Figure 11 shows an updated image of the IFR after 12 iterations which show more increased noise. This problem is known if we have an iterative solution algorithm and is called the semi-convergence phenomenon. It is similar to the semi-convergence phenomenon in algebraic reconstruction technique (ART), shown in Figure V.12 in [1]. It is a fundamental issue with methods that reproduce the measured data. The picture which best approximates the measured data may be a very noisy picture which is not the picture one wants. Thus, the best simulated data can come from a very noisy picture.

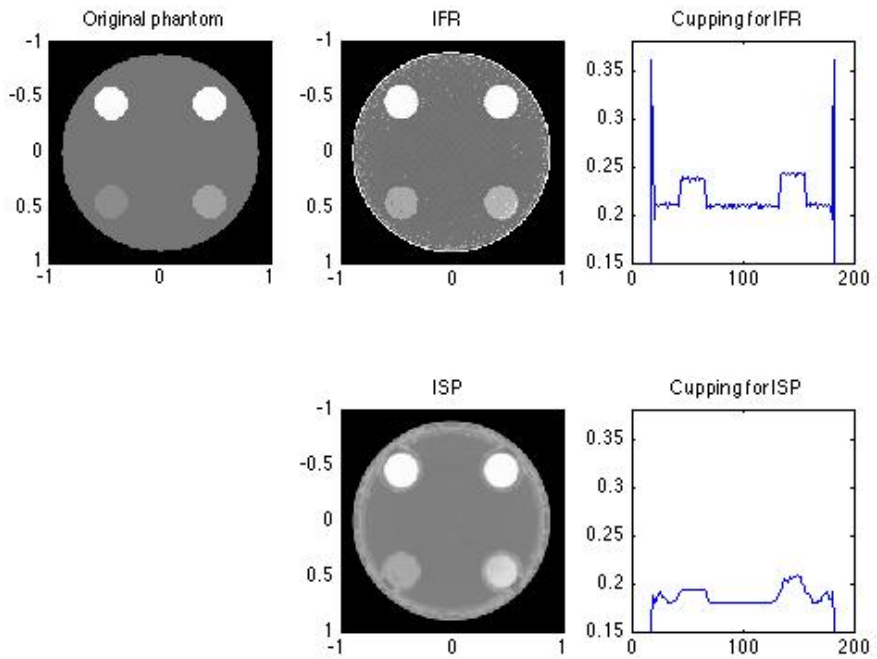

Figure 10: Illustration the performance of the two iterative algorithms IFR and ISP after 4 iterations. **Top left**: The original phantom as in Figure 9. **Top center**: A reconstruction image of the IFR algorithm. **Top right**: The corresponding density profile of row number 135 in the IFR image. **Bottom center**: A reconstruction image of the ISP algorithm. **Bottom right**: The corresponding density profile of row number 135 in the ISP reconstruction image. The grey scale window is [0.15,0.28] for IFR, [0.14,0.22] for ISP.

Table 3: Cost function results of IFR and ISP

Iteration	IFR	ISP
1	0.0411	0.0488
2	0.0231	0.0574
3	0.0180	0.0497
4	0.0158	0.0430
5	0.145	0.0414
6	0.0115	0.0460
7	0.0105	0.0358
8	0.0097	0.0395
9	0.0093	0.0354
10	0.0088	0.0270

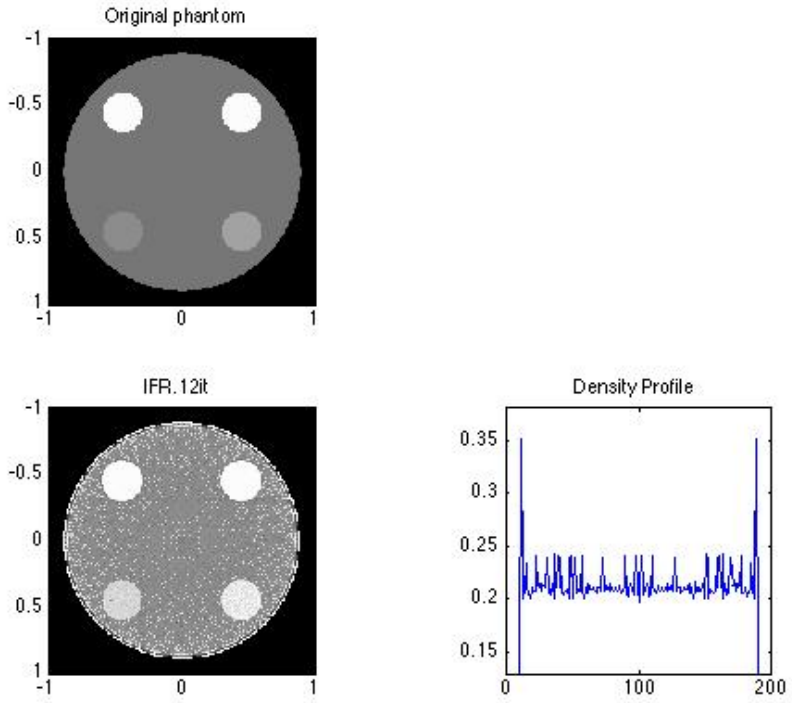

Figure 11: Illustration of semi-convergence phenomenon for the IFR after 12 iterations. **Top**: The original phantom as in Figure 9. **Bottom right**: A high noise reconstruction of the IFR algorithm after 12 iterations. The grey scale window is [0.16,0.25]. **Bottom left** : The density profile of row number 100 in the IFR image where high noise can be found.

Furthermore, we carried out an experiment to examine if the first stage of Herman and Trivedi improves the result of ISP algorithm. Figure 12 shows a comparison between the reconstruction from the ISP method and the corresponding image after running the first stage on that image. As shown in the density profile of the first stage, the overshoot in the boundary has been reduced but there is a bulge in the interior.

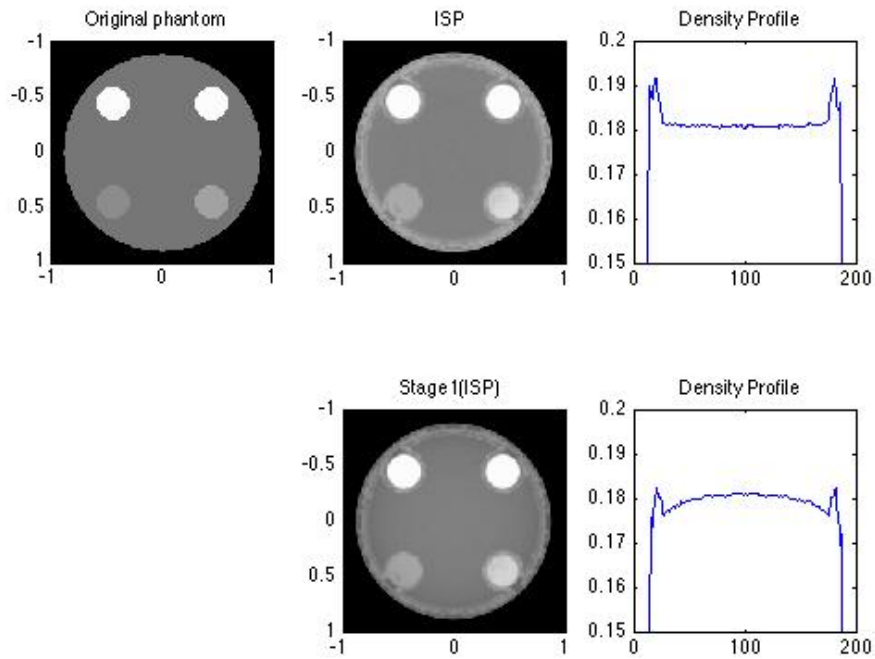

Figure 12: Illustration of using the first stage of correction after the ISP method. **Top left**: The original phantom as in Figure 9. **Top center**: ISP reconstruction after 4 iterations. **Top right**: The density profile of row number 120 in the ISP image shows overshoot in the boundary. **Bottom center**: The reconstruction after running the first stage on the ISP image, where $\mu^s(\bar{E}) = 0.19$. **Bottom right**: The density profile of row number 120 where the overshoot at the boundary is reduced but there is a bulge in the interior. The grey scale window is [0.14,0.22]

Chapter 4

Comparison and discussion

Figure 13 illustrates the performance of the three different methods on a phantom of 5 materials including air. The method of Herman and Trivedi strongly reduces the beam hardening artifacts but the dark streaks are still faintly visible. The corrected image has not much noise, sharp boundaries and it resolves all the tissues. On the other hand, IFR and ISP successfully remove the dark streaks between bones. IFR produces a more noisy image than the low resolution ISP and the image of Herman and Trivedi. A white ring at the outer boundary of the object is present in IFR and ISP but not in Herman and Trivedi's image. The corresponding profile plots of the corrected images in Figure 14 further show the difference in performance between the three methods. We insert a horizontal line through the lower two discs to compare how each method can deal with two low contrast materials of soft tissues. In comparison, IFR gives a better contrast between the two low contrast soft tissues than the two other methods.

Figure 15 shows the results of applying all the three methods on the simple brain and bone phantom that we used for Herman and Trivedi's method. All the three methods are significantly reducing the beam hardening artifacts. The corresponding profile plots for each image are shown in Figure 16. We insert a horizontal line through the two lower discs of bone. The results from the plots indicate that the IFR method preserves the contrast between the bone and the brain, while the contrast is reduced in the other two methods.

One of the main drawbacks of Herman and Trivedi's method is the longer computational time that it takes when compared to the two iterative algorithms. The two stages take 111 seconds to perform the full correction, while the IFR takes only 21 seconds, and the ISP takes 14 seconds.

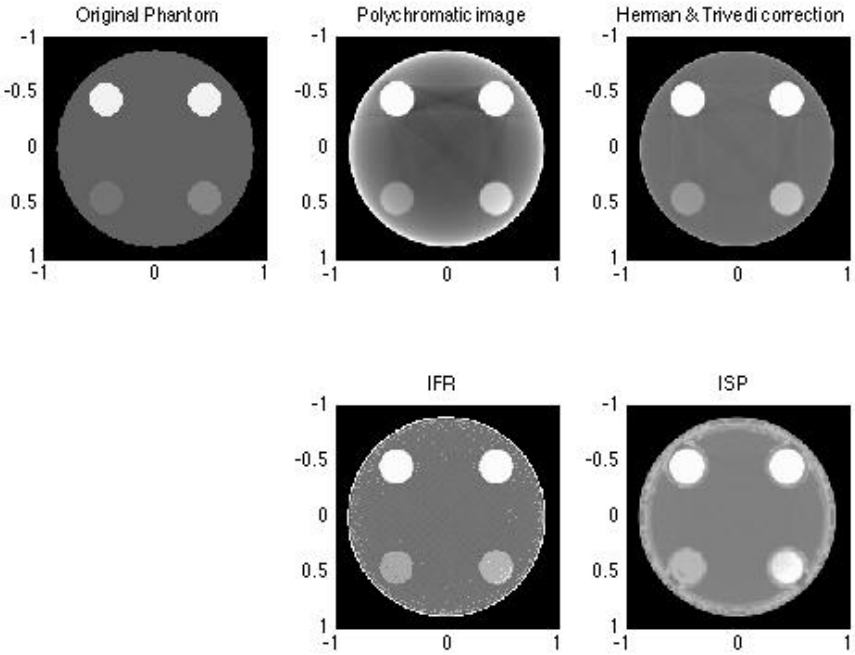

Figure 13: Reconstructions for all the three methods on the 5 materials phantom. **Top left**: The original phantom as in Figure 9 with (5 materials including air). **Top center**: Uncorrected polychromatic data with beam hardening artifacts with grey scale window [0.17, 0.20]. **Top right**: Herman and Trivedi correction with grey scale window [0.17,0.21]. **Bottom center**: The reconstruction from the IFR algorithm after 4 iterations with grey scale window [0.15,0.28]. **Bottom right**: The reconstruction from the ISP algorithm after 4 iterations with grey scale window [0.15,0.21].

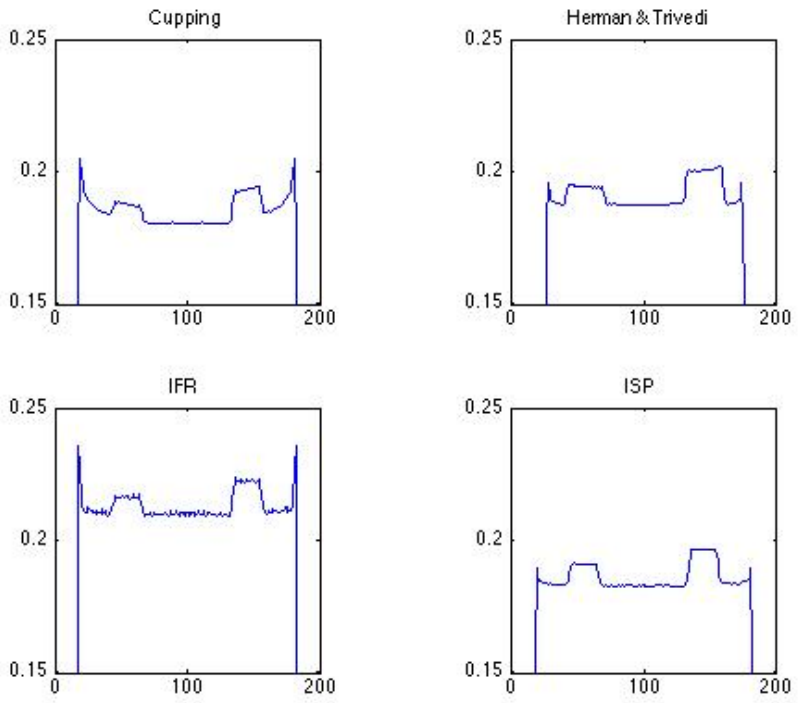

Figure 14: Density profiles for row number 135 in the reconstruction images shown in Figure 13. **Top left**: The density profile corresponds to the uncorrected polychromatic image where cupping artifact can be found. **Top right**: The density profile corresponds to the corrected image by Herman and Trivedi's method. **Bottom left**: The density profile for the IFR method. **Bottom right**: The density profile for the ISP method.

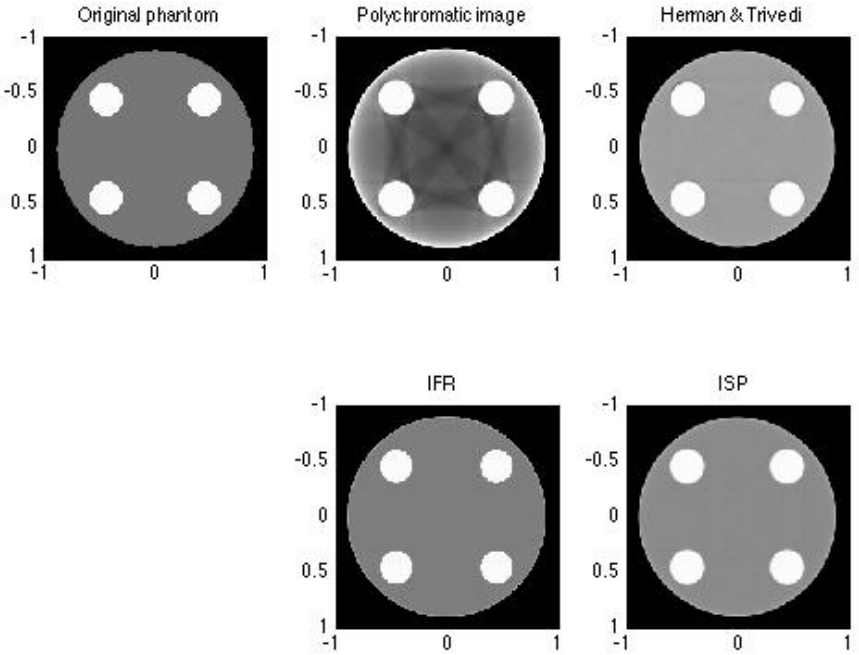

Figure 15: Reconstructions for all the three methods on the first phantom used in Figure 1. **Top left**: The original phantom as in Figure 1 with 2 materials (brain and bone). **Top center**: Uncorrected polychromatic data with beam hardening artifacts with grey scale window [0.17, 0.20]. **Top right**: Herman and Trivedi correction with grey scale window [0.17,0.21]. **Bottom center**: The reconstruction from the IFR algorithm after 4 iterations with grey scale window [0.15,0.28]. **Bottom right**: The reconstruction from the ISP algorithm after 4 iterations with grey scale window [0.15,0.21].

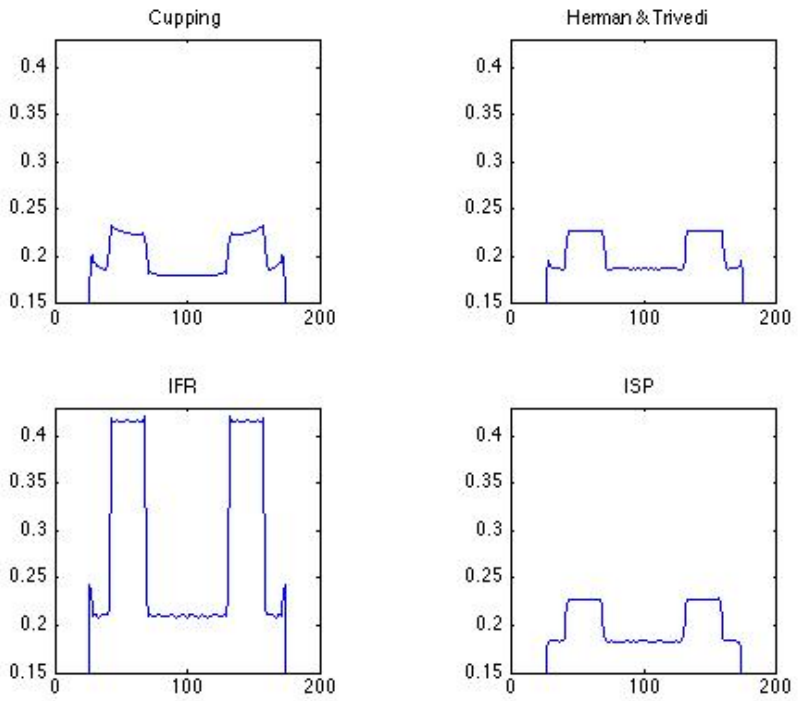

Figure 16: Density profiles for row number 150 in the reconstruction images shown in Figure 15. **Top left**: The density profile for the uncorrected polychromatic image where cupping artifact can be found. **Top right**: The density profile for the image corrected by Herman and Trivedi's method. **Bottom left**: The density profile for the IFR method. **Bottom right**: The density profile for the ISP method.

In this paper, the three methods that we presented aim to reduce beam hardening artifacts based on a discretized model for polychromatic data. All are post-reconstruction approaches. They all need an initial reconstruction and the original polychromatic data. In Herman and Trivedi's method, the goal is to generate artificial monochromatic data from the measured polychromatic data. It is initialized with an uncorrected image from the measured polychromatic data which is used to estimate the length of intersection of each material with each ray. It requires a segmentation of a preliminary image. The method is not iterative and has a two stage process. The image is obtained by reconstruction from the artificial monochromatic data. The numerical expiremnts indicated that the method successfully reduced cupping and dark streaks artifacts for an object of two materials (refer to Figure 6). For more than two materials, both artifacts are still reduced but not as well as for two materials as shown in Figures 13 and 14. The method does not seem to introduce much noise. The corrected image is sharper than ISP and about as sharp as IFR. A limitation of the method is that it needs more computational time than the other two methods since it requires to solve two nonlinear equations in one variable for each ray.

The two iterative algorithms IFR and ISP are designed for an arbitrary but known number of materials. Both require segmentation in every iteration. The IFR aims to find an image whose simulated polychromatic data are close in the l_2-sense to the measured polychromatic data. The image is obtained from the segmentation by assigning suitably chosen density values to each material. These values are then multiplied for each pixel by the corresponding relative density value. IFR allows for non-uniformities in a material's density which is considered a practical advantage compared to the other two methods. Our result illustrated that the IFR sufficiently reduced beam hardening artifacts. The corrected image is sharp. The relative density parameter appeared to be able to compensate somewhat for misclassifications in the segmentation. After further iterations, the semi-convergence phenomenon was observed where images become more noisy. The authors recommend to smooth the image before segmentation to control this noise. Numerical challenges were encountered with minimizing the cost function with respect to thresholds for segmentation. To avoid that, we used a heuristic method but further refinements may be needed. TISPhe IFR is fast but not guaranteed to decrease the cost function. We did not implement the much slower method that updates the relative density by minimizing the

cost function. The ISP is a sinogram preprocessing method and aims to find artificial monochromatic data. Unlike the IFR method, the ISP assumes the materials to be uniform. The image is obtained from a reconstruction from the artificial monochromatic data. Information about low-contrast materials that may be misclassified in the segmentation is contained in the contribution of the original measured data to the artificial monochromatic data. The results indicated that the ISP works well on two materials. It produced sharp images. Cupping and dark streaks were removed. For five materials (including air), the ISP also removes cupping and streaks but the image is not as sharp as for the other two methods. It introduced a new ring-shaped artifact near the boundary of the object. The other two methods have also such an artifact but the ring is much thinner. The ISP is the fastest compared to the other two methods.

References

[1] F. Natterer, The Mathematics of Computerized Tomography, SIAM, Philadelphia, PA, USA, 2001.

[2] G. T. Herman, Image reconstruction from projections: the fundamentals of computerized tomography, Academic Press, New York, 1980.

[3] G. Herman and S. Trivedi, "A comparative study of two post-reconstruction beam hardening correction methods," IEEE Trans. Med. Imaging 2,128-135 (1985).

[4] G. Van Gompel, K. Van Slambrouck, M. Defrise, K. Batenburg, J. de Mey, J. Sijbers, and J. Nuyts, "Iterative correction of beam hardening artifacts in CT," Med. Phys. 38, (2011), pp. S36-S49.

[5] The MathWorks. http://www.mathworks.com/help/images/ref/radon.html

[6] The Nobel Prize in Physiology or Medicine 1979. Available online at www.nobelprize.org

[7] M. Krumm, S. Kasperl, and M. Franz, "Reducing non-linear artifacts of multi-material objects in industrial 3D computed tomography," Nondestr. Test. Eval. 41, 242-251(2008).

[8] N. Rezvani, "Iterative reconstruction algorithms for polyenergetic x-ray computerized tomography," Ph.D. thesis, Graduate Department of Computer Science, University of Toronto, Toronto, Canada, 2012. Available online at www.cs.toronto.edu/pub/reports/na/Nargol.Rezvani.PhD.Thesis.pdf

[9] P. Joseph and C. Ruth, "A method for simultaneous correction of spectrum hardening artifacts in CT images containing both bone and iodine," Med. Phys. 24, 1629-1634(1997).

[10] P. M. Joseph and R. D. Spital, "A method for correcting bone induced artifacts in computed tomography scanners," J. Comput. Assist. Tomogr. 2, (1978), pp. 100-109.